Composites Science and Technology 195 (2020) 108163

Contents lists available at ScienceDirect

Composites Science and Technology

journal homepage: www.elsevier.com/locate/compscitech

3D interfacial debonding during microbond testing: Advantages of local strain recording

R. Dsouza [a,*], P. Antunes [d,e], M. Kakkonen [b], J. Jokinen [a], E. Sarlin [a], P. Kallio [c], M. Kanerva [a]

[a] Tampere University, Faculty of Engineering and Natural Sciences, PO Box 589, FI-33014, Tampere, Finland
[b] Fibrobotics Oy, Korkeakoulunkatu 1, 33720 Tampere, Finland
[c] Tampere University, Faculty of Medicine and Health Technology, PO Box 589, FI-33014, Tampere, Finland
[d] Instituto de Telecomunicações, PO Box 3810-193, Aveiro, Portugal
[e] Physics Department and I3N, Aveiro University, Campus de Santiago, PO Box 3810-193, Aveiro, Portugal

ARTICLE INFO

Keywords:
Glass fibres
Finite element analysis (FEA)
Cohesive zone modelling
Debonding
Interface

ABSTRACT

The microbond (MB) test is the most widely adopted micromechanical test to characterize fibre matrix interfaces but typically lacks reliability and output for determining multi-parameter interface models. In the current research, the MB test is enhanced by incorporating Fibre Bragg Grating (FBG) sensors for local fibre strain monitoring. Strain-force data is used to analyse and validate the type and paramter values of a cohesive zone modelling (CZM) basis in the three-dimensional interface damage model. For the prepared epoxy resin droplets, that are used as a benchmark case, a bi-linear CZM traction-separation law is fitted for each droplet. The results confirm the selection of maximum FBG strain, force–strain profile with the two primary peaks in the force–strain derivative, and the peak force to be valid for proper interface characterization. The analysis of the performed tests clearly reveal the droplet fracture process to consist of four distinct stages. Only after the first stage, interfacial crack propagation independent of the point on perimeter is achieved. Full debonding occurs during the fourth stage.

1. Introduction

The fibre matrix interface significantly affects the static strength in the transverse and compressive directions and in general laminate damage propagation under dynamic loads [1,2]. Additionally, the anticipated interphases have an influence on the diffusion and ageing behaviour of composites [1].

The adhesion and related mechanical strength between matrix and the fibre surface is the corner stone of composite integrity and the standpoint of micromechanical models. Microbond (MB) or micro droplet - tests, resin pull-out tests and fibre push-out tests are the current experimental methods in microscale for studying the adhesion of fibre matrix interfaces [3]. The testing must be done on fibres specifically due to the fact that the surface chemistry and morphology are unique in drawn fibres compared to flat, identical plates in terms of composition, for example.

The current interface test methods can output force and the (blade) displacement data. For basically all practical implementations, the displacement data is based on a control signal (of loading blades or a clamp [4–6]) and not a precise displacement transducer (e.g. micro-LVDT) near the interface. Therefore, in addition to inevitable system compliances, the output in terms of 'displacement' is essentially inaccurate of the real interfacial deformation. In general, cross-head displacement is basically never used for valid measurements in standard fracture testing of interfaces and joints [7,8].

The current measures of fibre matrix interfacial adhesion rely on single output, the maximum force value of the test. Thus, for analysis, whether based on a stress or energy basis, only single parameter solutions have been published [6,9,10]. Because the interfacial fracture is a multi-stage process, inclusive of various nucleation and propagation related phenomena, a unitary test output cannot be used to determine the process constants regardless of the test series (sample) size [11] and related statistical reliability. Optical strain measurements have been applied for MB tests using Raman [12] or embedded Fibre Bragg grating (FBG) sensor [13] but the inherent scatter has not allowed proper strain output in the neighbourhood of the interface.

This work introduces the local strain as an additional measure for MB testing. This is the first time when full-scale three-dimensional (3D) finite element (FE) modelling and accurate force–strain data from microbond tests is analysed in detail with a significant resolution of crack nucleation and fracture evolution phenomena at the interface.

* Corresponding author.
E-mail address: royson.dsouza@tuni.fi (R. Dsouza).

https://doi.org/10.1016/j.compscitech.2020.108163
Received 9 October 2019; Received in revised form 25 March 2020; Accepted 4 April 2020
Available online 10 April 2020

2. Microbond samples and preparation

The experimental setup of the MB test is shown in Fig. 1. Silica optical FBG sensor is used for the test, and they were tailored by Instituto de Telecomunicações (Aveiro, Portugal). A step index single-mode glass fibre (GF1, Nufern®) is used, with core and cladding diameters of 10 μm and 125 μm, respectively. FBGs (3 mm long grating), separated with a 10 mm gap and spectrally separated by 5 nm, were inscribed in the same fibre using the phase mask method [14].

Droplets of different sizes were prepared by a developed resin dip method using a mixture of Araldite® LY 5052 as resin and Aradur® 5052 as hardener (Huntsman), with a mixing ratio of 100/38 (mass/mass). Droplets were carefully positioned taking into consideration the positions of the FBG sensors in the optical fibre. Both FBG sensor and the blades were always located in front of a droplet because the blades must push against the droplet, thus, the FBG sensor always experiences tensile strain. Droplets were cured for 48 h at 27 °C. The experiments were carried out using a FIBRObond (Fibrobotics, Finland) micro-droplet tester [11]. The tester involves 1 N and 5 N load cells (used respectively based on the droplet size), surgeon knives (R35, thickness 0.254 mm, Feather, Japan) for droplet loading, and an electrical linear motor to load the droplet. The tests were performed at a constant displacement rate of 0.08 mm/s until full failure (debonding) of a droplet. Separate experiments and respective simulations were carried out for five different droplets. The geometrical features of each droplet were captured before testing using the optical camera (model UI-3370SE, IDS, Germany) of the FIBRObond tester. The strain acquisition system for the FGBs was a W3/1050 Series Fibre Bragg Grating Interrogator (Smart Fibres®) with a wavelength range of 1510–1590 nm and accuracy of ±0.0006 nm. The interrogator was operated using a Remote Interface W3 WDM (version 1.04) at a sampling rate of 50 Hz. After testing, scanning electron microscopy (SEM) was carried out (model ULTRAplus, Zeiss, Germany). Prior to SEM studies, the droplets were coated with a thin layer of carbon to avoid charging (see Fig. 9).

3. Numerical model and analysis

3.1. Finite element model

Full 3D FE models were developed using Abaqus/Standard 2017 (Dassault Systèmes). Each model assembly consisted of the droplet, fibre, blades, connection adhesive and the entire sample holder. The fibre, adhesive and the sample holder were assumed to behave along the linear-elastic regime. In turn, each droplet was modelled with an elastic–plastic behaviour via kinematic hardening conditions. The steel blades were treated as rigid body elements with displacement as an input during simulation. The material constants are shown in Table 1. The material properties except for the epoxy droplet were provided by the manufacturer. The shape of each droplet was determined based on optical data taken by the tester (2). The processed data points were imported to Abaqus, giving the true shape of each droplet. For data comparison, a section of elements (same length as that of the true FBG sensor) was defined to extract the simulated strain response.

The fibre model was constrained to the adhesive model as well as to the sample holder model using the so-called tie constraint. The sample holder model was constrained for all DOFs at the contact points. (see Fig. 2). A frictionless and hard contact was modelled as contact functions between the droplet models and the two blade models. The blades were constrained in all directions except for the z-axis, as shown in Fig. 2. Cohesive zone modelling (CZM) was employed to create the interface between the droplet models and the two blade models. The final FE assemblies consisted of 80,083–97,627 elements depending on the droplet mesh. At a maximum, a mesh of 309,628 elements was analysed to check the effects of mesh density [16].

Table 1
The values of the material constants used in the FE modelling in this study.

Part	Modulus (GPa)	Poisson's ratio	Element type
FBG Fibre	70	0.22	8-node linear brick (C3D8R)
Epoxy[a]	3.2	0.35	8-node linear brick (C3D8R)
Blades[b]	220	0.29	8-node linear brick (C3D8R)
Sample holder	3.2	0.37	4-node linear tetrahedron (C3D4)
Adhesive	1.6	0.29	4-node linear tetrahedron (C3D4)

[a]Plastic strain evolution with discrete steps (0%, 60 MPa; 0.2%, 70 MPa) [15].
[b]Modelled as a rigid body.

3.2. Interface model: surface-based cohesive behaviour

To consider the damage and failure of the interface region, a bi-linear traction-separation law was employed in the form of [17]:

$$\sigma = \begin{cases} K\delta & for \quad \delta \le a_0 \\ \frac{a_1-\delta}{a_1-a_0}\cdot\sigma_0 & for \quad a_0 \le \delta \le a_1 \\ 0 & for \quad \delta \ge a_1 \end{cases} \tag{1}$$

where $a_0 = \sigma_0/K$ and $a_1 = 2G_c/\sigma_0$. For the interface, σ_0 defines the damage onset, K the cohesive stiffness prior to damage onset, δ the contact separation, and G_c the energy of debonding for a mixed-mode fracture. The current interface model utilizes a maximum stress criterion (Eq. (2)) for the damage onset and a mixed-mode power law criterion (Eq. (3)) for the damage evolution. The subscripts s, t, and n are the first and second orthogonal in-plane shear and out-of-plane normal components of the traction vector in the contact element coordinate system, respectively. The mode I component was assumed to behave similarly with the mode II and mode III for G_c and τ:

$$max\left\{\frac{\tau_s}{\tau_{s_{cr}}}, \frac{\tau_t}{\tau_{t_{cr}}}, \frac{\tau_n}{\tau_{n_{cr}}}\right\} = 1 \tag{2}$$

$$\frac{G_I}{G_{I_{cr}}} + \frac{G_{II}}{G_{II_{cr}}} + \frac{G_{III}}{G_{III_{cr}}} = 1 \tag{3}$$

Here, the CZM model was fitted for each droplet (presuming variation in the real interface constants) with the related 'debond strain' (ε_{max}) as a primary target value and the 'maximum force' ($F_{max} = F_d$) as a secondary target value. The simulated F_d value was assumed to involve some deviation from an experimental value due to FE models typically slightly lack compliance. Initial estimates of the fracture energy were calculated by the shear lag model according to Scheer and Nairn [18].

4. Results and discussions

4.1. Experimental results of microscale fracture

Fig. 3(a) and (b) present the strain and force output obtained from the experiments. The plot consists of the experimental results of five different droplets of varying embedded length and droplet diameter (see Table 2). Strain–time and force–time graphs exhibited a very slight kink per droplet, labelled as ε_{kink_i} and F_{kink_i} *(i=1 to 5)*, respectively. The force (F_{max_i}) and strain (ε_{max_i}) monotonically increased up to a maxima followed by a sudden failure (final debonding of the droplet), as indicated in Fig. 3. When a droplet debonds, the force transfer via interface ceases to be, i.e., force drops close to the zero level. In some cases, friction or deformation of the meniscus sustain a slight force level. The overall force–strain curve is shown in Fig. 4 for Droplet 3. The corresponding experimental and simulated force–strain data for all the droplets (Droplet 1, 2, 4 and 5) are given in a report [16]. A comparison of the peak load of debonding (i.e. F_d) with the embedded area per droplet indicates that a good range of embedded lengths was used here to verify the findings in general [16].

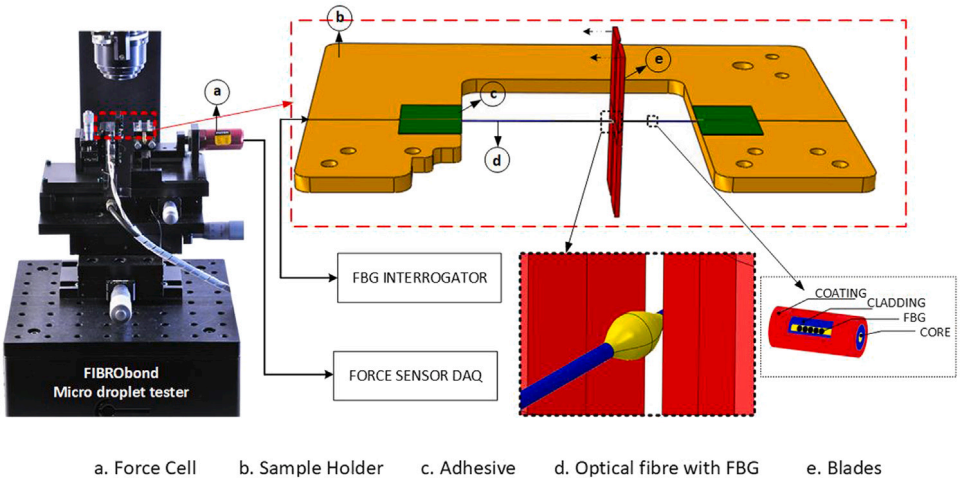

Fig. 1. Experimental setup of the MB test.

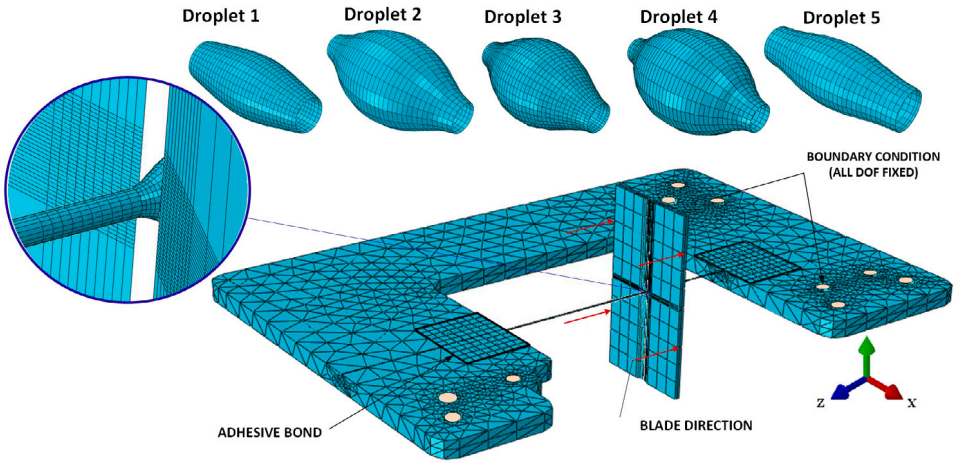

Fig. 2. FE modelling of the MB test system and the different droplets.

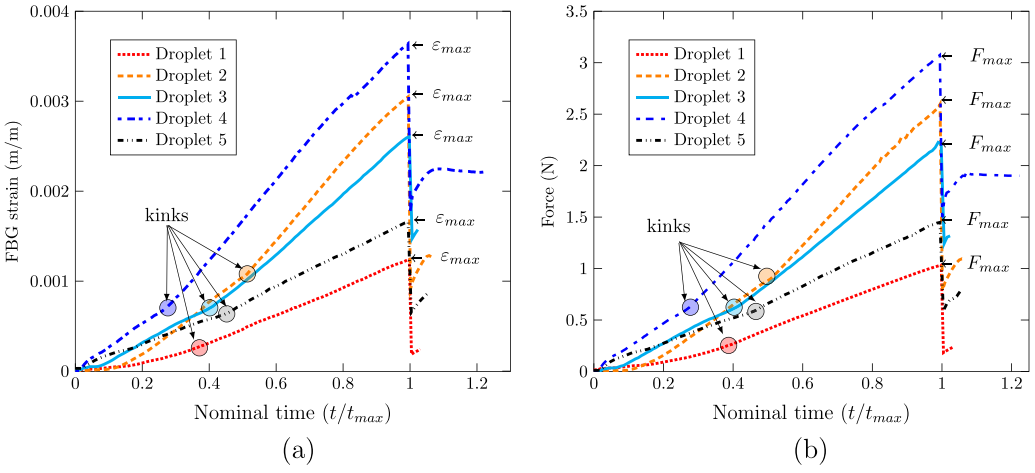

Fig. 3. Experimental raw data for five different droplets: (a) strain–time graphs for different droplets; (b) force–time graphs for different droplets.

4.2. Interfacial behaviour and related material constants

From the well-known Shear lag equations [18], we obtained a value of 42 J/m^2 as the trial value of fracture energy G_c (for Droplet 3). Further more, three different combinations of G_c and τ were considered and compared to experimental results, as shown in Fig. 4. It should be noted that there could be several combinations of G_c and τ for which the simulated peak force fits the experimental peak force. Fig. 5(a)

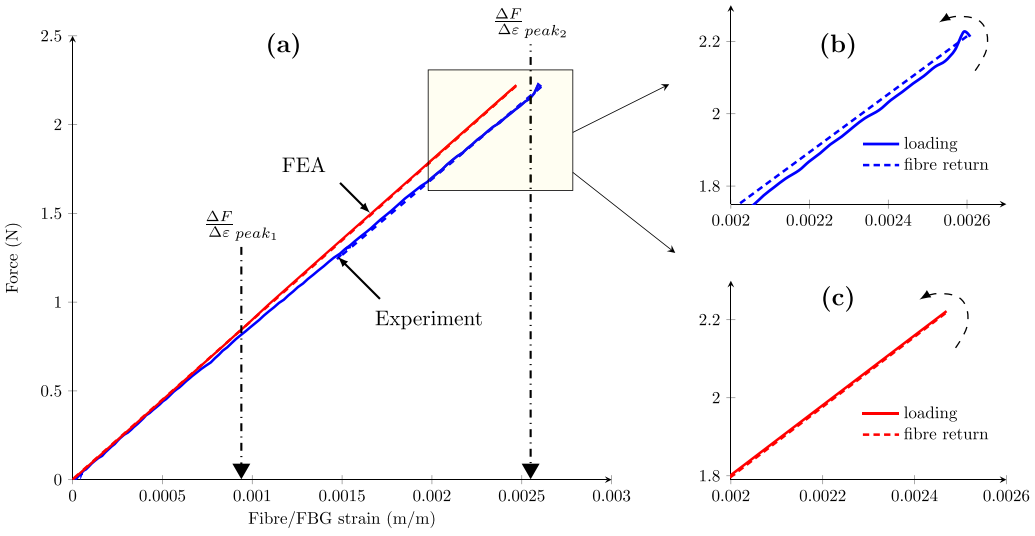

Fig. 4. (a) Force–strain behaviour during MB test of Droplet 3; (b) the experimental curve for the selected section; (c) the simulated curve for the selected section.

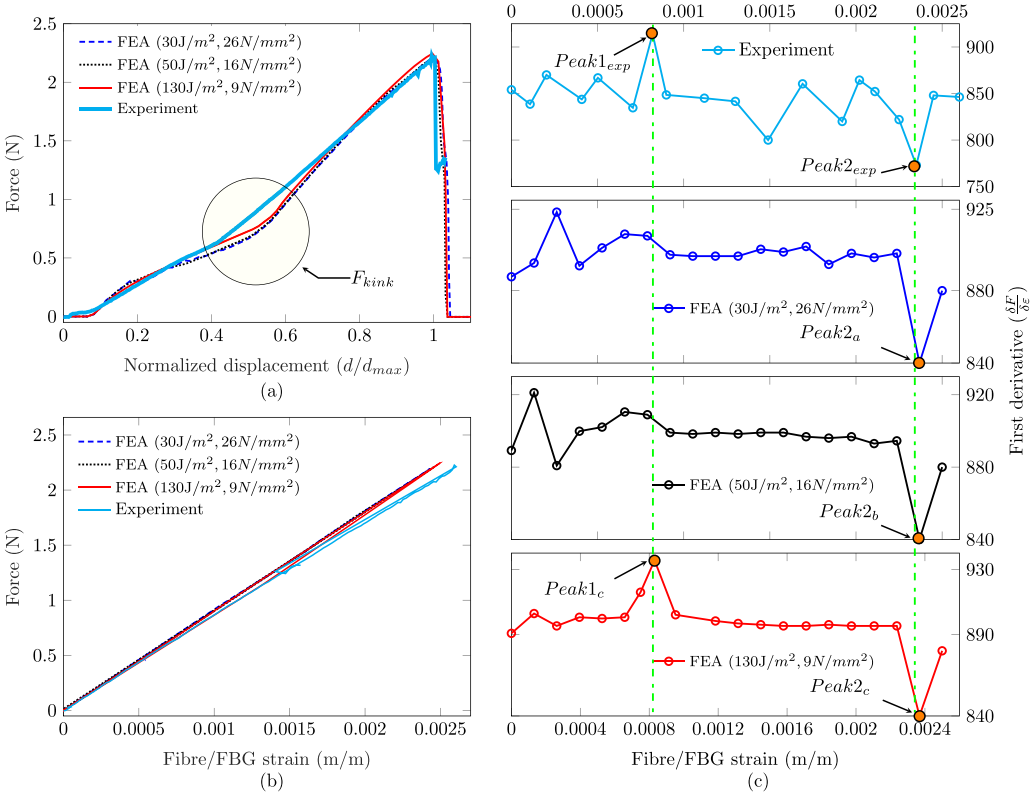

Fig. 5. The iteration of values of G_c and τ_{cr} in comparison with the experimental results for Droplet 3; (a) force versus normalized displacement; (b) force versus strain; (c) the first derivatives of force–strain data.

Table 2
Determined dimensions of the droplets and the fitted interface constants.

Droplet (diameter, embedded length l_e) (mm)	Critical τ (MPa)	G_c (J/m^2)
1 (ø=0.218, l_e=0.561)	9	41
2 (ø=0.384, l_e=0.731)	10.5	130
3 (ø=0.376, l_e=0.687)	10	130
4 (ø=0.452, l_e=0.786)	11	130
5 (ø=0.206, l_e=0.524)	11	85

shows the simulated reaction force over the displacement. It is evident that the test (Droplet 3) could have several combinations of G_c and τ. Interestingly, the kink (F_{kink}) observed with the different G_c and τ values have similar features. It is interesting to note that the position of the kink also varies with the blade's initial position (contact point with the droplet) and it is important to define the position for the tests performed in practice [19]. Fig. 5(b) shows the force–strain curves and Fig. 5 (c) shows the first derivative curves of the force–strain data (G_c and τ values surveyed). The experimental force–strain derivative shows two major peaks (*Peak*1 and *Peak*2) representing local maxima and

minima, respectively. As an example, the experimental $Peak2$ best coincides with all three iterations (FEA) whereas the first peak ($Peak1$) is only reproduced by the third numerical iteration. With higher values of τ, the second peak is observed for all the value combinations, whereas the first peak is observed only with a higher G_c (130 J/m^2). Upon studying the stress distribution at the interface (Droplet 3), a smooth exponential decay of the shear stress (along the fibre co-ordinate) with the value of G_c = 130 J/m^2 was observed [19].

During the damage process of interface, a droplet undergoes plastic deformation. Although the elastic limit is here a known parameter, the hardening laws play a major role. Naturally, a single force parameter cannot be used for confirming the proper hardening. Here, classical plasticity with kinematic hardening condition was observed to match experiments and was tested for various conditions (elastic–perfectly plastic, elastic–plastic with isotropic hardening and elastic–plastic with kinematic hardening conditions). Each of the cases were tested for the fitting; the process involving the maximum peak force as well as maximum peak strain, and the kink strains in the derivative. The most accurate fitting was found with the third case of hardening law where the maximum strain and force matched the experimental values. In addition, SEM imaging was used to verify the final, permanent deformation of the droplet and in comparison with the simulated deformation.

4.3. Features revealed by force–strain data analysis

Due to the fact that a MB test mostly shows tensile behaviour of the fibre, the interfacial phenomena are mainly revealed by the first and the second derivatives of the force–strain curves. The interfacial loading along the CZM regime contributes only ≈8% of the strain energy whereas the rest of the strain energy is stored in the other parts of the model, primarily in the bulk droplet and the fibre.

The first derivatives of two example droplet samples are shown in Fig. 6(a–b) and Fig. 6(f–g), respectively. To understand the division between the simulated damage in the droplet and the fibre-droplet interface, the energy curves from the FE simulations must be monitored and compared to the experimental force–strain data. Moreover, the law of conservation of energy must be confirmed before a detailed analysis. To study the detailed characteristic features of the MB test, curves are considered only until the debonding. By considering the entire process to be quasi-static prior to the final debonding of a droplet, the energy balance can be written as $\sum E_{prior} = \sum E_{after}$. Here, $E_{contact} = E_{DMD} + E_{IE}$, where E_{DMD} is the energy dissipated at the established cohesive interface, and E_{IE} is the internal energy of the rest of the model during the simulated test. Also, $E_{IE} = E_{SE} + E_{PD}$, wherein E_{PD} is the energy dissipated by the plastic deformation of the droplet's polymer and E_{SE} is the recoverable strain energy. It can be seen that the 1st derivative peaks match with the evolution of the energy division by FE analysis, as shown in Fig. 6(c) and (h). The derivative curves and the energy curves for Droplet 3 and Droplet 4 are presented in a report [16].

When the blades initially come in contact with a droplet, external work is being done to the system. Due to the deformation in a droplet (elastic–plastic), energy is gradually stored and finally, used for plastic deformation. As the traction-criterion at the interface exceeds the critical stress value (9 MPa for Droplet 1 and 10.5 MPa for Droplet 2), interfacial damage onsets with a marked energy consumption. For clarity, only the loading phase until debond is considered in the interpretation (more data in a report [16]).

Let us consider the first test (Droplet 1), as shown in Fig. 6. The first derivatives of force–strain curves (experimental and FEA) indicate two significant peaks ($Peak1$ and $Peak2$). There are only slight irregularities seen in the energy dissipation due to the interfacial behaviour. From the simulation, it was verified that this distortion is not affected by the selected traction or critical fracture energy values. Merely the geometry of the droplet and blade contact affect these deviations. It is worth noting that the volume fraction of Droplet 1 is lower than that of the fibre ($V_1 > V_2$ as defined in a report [16]). Finally, a large change in the rate (slope) of interface damage is indicated at two distinct strain levels: 0.04% and 0.107% (Fig. 6(c)). The energy dissipated due to the plastic deformation of the droplet is increased over the strain range from 0 to 0.04%, as given by a sudden change in the slope.

Indeed, there is an abrupt change in the slope after the 0.107% of fibre strain. The reason can be better understood via the areal interfacial damage, as shown in Fig. 6(c). At the point E_{DMD_1}, the interfacial damage has spatially covered the circumferential direction of the droplet-fibre surface near the fibre entry to the droplet. At the point of ≈33% of the process time/displacement, a thorough crack nucleation around the fibre is achieved. At this transition point, the energy of interfacial damage (by E_{DMD_1} and E_{DMD_2}) is suddenly increased. After this point, the essentially abrupt debonding occurs (i.e., the front of open crack propagates). Overall, an amount of strain energy (of 0.011 mJ, in Fig. 6(d)) is stored in the system during the loading process and ≈20% is transmitted to the interface (Fig. 6(e)). The internal energy and strain energy of the entire model involve a significant slope-change at E_{IE_1} and E_{SE_1}, which corresponds to $Peak1$.

In comparison, the large Droplet 2 (with different V_1/V_2) has similar behaviour as Droplet 1 except for the fact that the energy curves have much smoother transitions. As the blades come into contact with the droplet, the plastic energy dissipation grows in a smooth polynomial fashion up to 0.10% of strain (Fig. 6(h)). Then, the curve exponentially evolves until the 'debond force' peak (F_d). The damage at the interface dissipates energy with a nonlinear growth, starting at a 0.10% of strain (E_{DMD_1}). The interfacial damage energy once again rises abruptly at a point of 0.28% strain (E_{DMD_2}) that is the main contributing factor for the position of $Peak2$ (FEA) in the 1st derivative curve. The absolute strain energy (SE) of the entire model is higher compared to Droplet 1 and also the portion of strain energy at the interface is significantly higher but the relative strain energy along the interface tends to decrease with an increase in the droplet volume (within the size regime studied here).

4.4. Fracture process at fibre-droplet interfaces

There are two significant features, which were observed for all the samples, with all of the force–strain derivative curves and the simulation data (energy consumption per damage mode). In summary, there is a good agreement of behaviour between Droplet 2, Droplet 3 and Droplet 4 because there is a small change in the volume of these droplets (also $V_1 > V_2$). In contrast, Droplet 1 and Droplet 5 have a lower volume fraction of the droplet. As the volume of the droplet increases, the strain energy for the entire model increases but the strain energy at the interfacial region decreases (Fig. 7). This suggests that the size of the droplet inevitably affects the practical accuracy of experimental data that should describe an interface. Fig. 8 shows the damage energy at the interface for all of the studied droplets as well as visualizes the crack propagation and stress accumulation along the interface.

The interfacial damage can be described in four stages of fracture:

- Stage 1: At this stage, the applied load on the droplet leads to fibre elongation and deformation of the droplet. There is no crack nucleation at the interface ($\tau_{cr} > \tau$).
- Stage 2: Now $\tau_{cr} = \tau$, hence damage is locally initiated near the blade location (see Fig. 8(f)). Damage progresses circumferentially with an increase in the rate of damage energy. At the end of the stage $\tau_{cr} \approx \tau$ wherein the damage rate has become constant as well as the growth of interfacial damage in the fibre's longitudinal direction (Fig. 8(g)). Typically, the MB tests loading has reached around 40% of the peak levels of force or displacement or fibre strain.
- Stage 3: The interfacial damage progresses and extends spatially in the fibre's longitudinal direction. A smooth transition of interfacial damage occurs from point ii to iii (as shown in Fig. 8(h)).

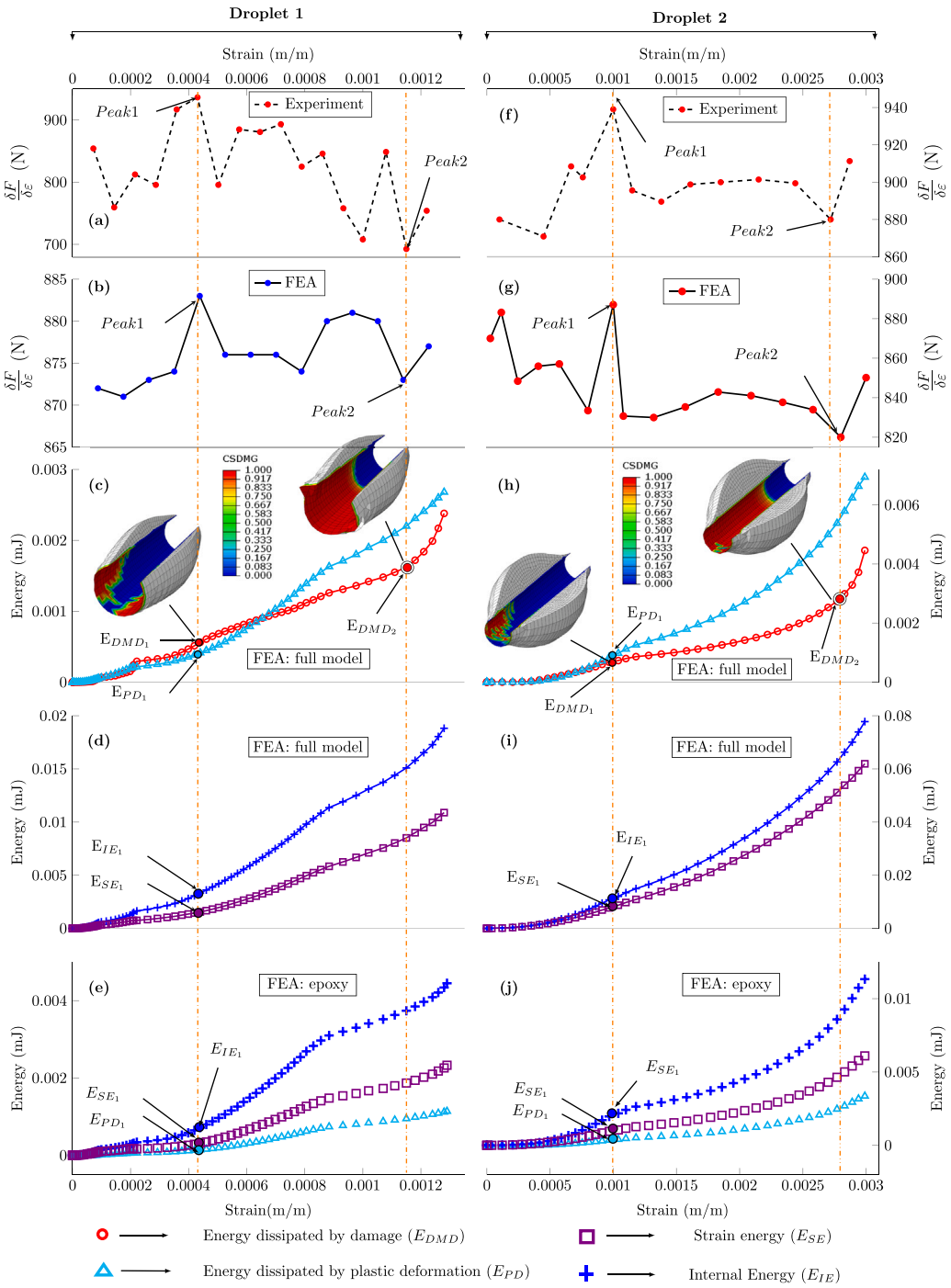

Fig. 6. (a,f) Experimental force–strain derivatives; (b,g) FEA of the force–strain derivatives; (c,d,h,i) FEA of the energy division for the overall model; (e,j) FEA of the energy division for the droplet volume.

- Stage 4: There is an abrupt rise in the consumption of interfacial damage energy; final debonding emerges and crack-front propagates towards the non-damaged last portion of the interface (the intact meniscus).

4.5. Fibre return movement at debonding

The position of the droplet along the fibre, during the MB test, can have significant effects on Stage 4 (in Fig. 8) due to the different amount of absolute deformation related to a critical level of load (and fibre strain). Droplets at three distinct positions are shown in Fig. 9. Based on the droplet position and fibre elongation during the fourth stage, there is no fibre return movement in Droplet 1 and 2 until the complete debond. As the fibre's loading length (i.e., distance of the point of blades from the sample holder) increases, the fibre's backward displacement already initiates during Stage 4 although the droplet yet has not debonded. For instance, Droplet 1 is closer to the fibre fixing point at the holder (s = 6.25 mm), hence deformation of the fibre (δ_f) is around 11 times the droplet's embedded length. The recoverable strain energy in the test of Droplet 3 begins to get released at Δa = 0.49 mm due to the deformation of 34.5 times the droplet size and the three times higher absolute return deformation needed to release the corresponding amount of energy (than for the location

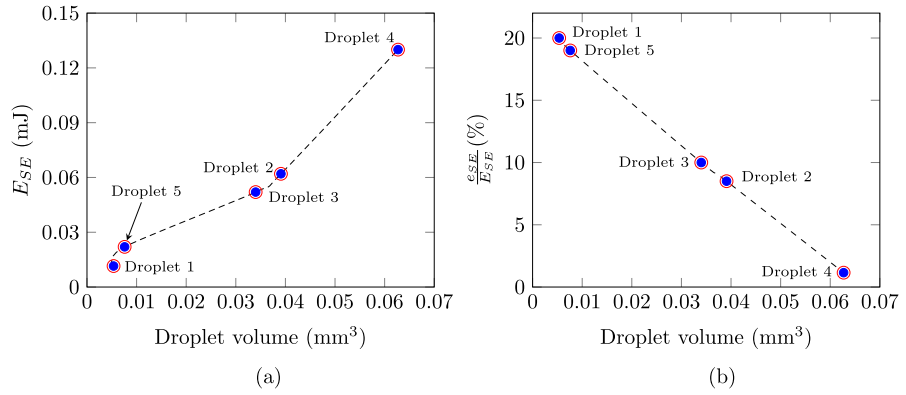

Fig. 7. Total strain energy versus droplet volume, at the MD test's point of debond strain (ε_{max}), (a) as given for the entire FE model (E_{SE}); (b) relative to the interface alone (e_{SE}).

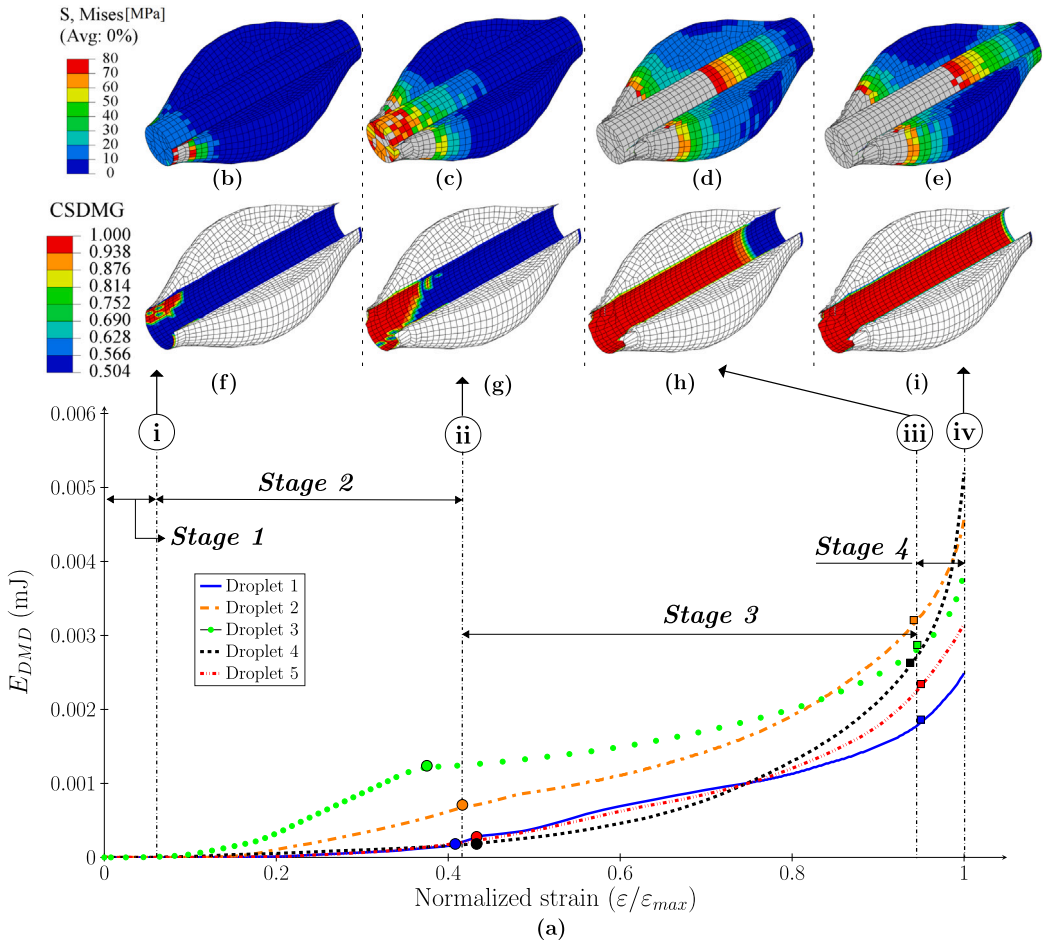

Fig. 8. (a) Energy dissipated at the interface for MB tests with four distinct phases of fracture; (b–e) global von Mises stress contours at 4 distinct locations i, ii, iii and iv respectively; (f–i) interfacial damage state (CSDMG) at 4 distinct locations i, ii, iii and iv respectively.

of Droplet 1). The backward displacement means that the recoverable energy will turn into kinetic energy of the fibre in real test. Based on Fig. 9, only for Droplet 3, slight dynamic effects at the end of Stage 4 could affect the behaviour. If interfacial damage is coupled with friction [20], these dynamic effects could also affect the fibre displacement.

4.6. Advantages of measuring local strains with FBG

As FBG sensors experience their local strain right ahead of the droplet, the sensor also allows one to get an exact stress–strain curve of the fibre with the droplets and over the entire (dynamic) range of a test. The effects of system lag, compliance and linear motor calibration have no effect during a measurement. Due to the proximity of the FBG sensor with the droplets, its readings are clearly more sensitive to slight interfacial mechanics than the load cell—the load cell being typically

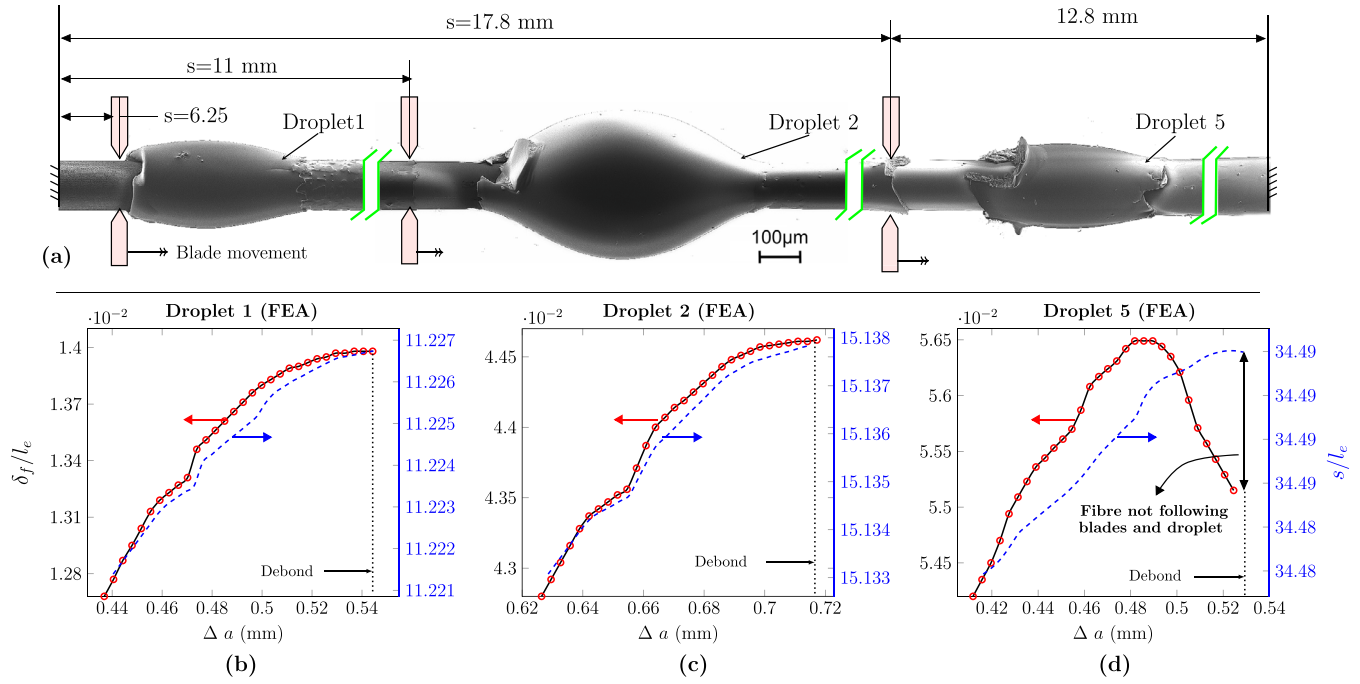

Fig. 9. (a) The SEM images of the Droplets 1, 2 and 5 and their respective position along the fibre; (b–d) the fibre displacement from the initial position of blades (δ_f) and blade distance from holder (s) as a function of crack growth ($\Delta\ a$) for different droplet sizes during Stage 4.

connected to relatively large system masses (e.g. sample holder unit or blade unit). Additionally, a fibre only carries axial loads similarly to the FBG readings making the local strain monitoring independent of friction or calibration due to a 'primary' measuring direction (such as in a load cell or displacement transducer).

5. Conclusion

This paper investigates the use of local strain by using optical fibres as an additional output during MB testing and analyses the full-field three-dimensional behaviour via finite element simulations. The results reveal that all the three outputs are not only useful but crucial in resolving the interface fracture problem: peak strain, peak force, and the first derivative of the force–strain profile. Thus, a single solution for finite element methods was defined for the fibre droplet interface by applying fracture toughness and critical traction as well as the validation of model's stiffness. For FBG sensor application with an optical fibre and epoxy droplets, the test setup is able to clearly reveal the four fundamental stages of fracture: reversible (elastic) loading regime, crack nucleation, growth and full debond. For the interface between optical fibre and epoxy, precise fracture toughness and critical traction values per droplet were determined. Many of the previous models rely on a single parameter, not least because of the long history of load being the most precise test output. Based on the work here, any bi-linear interface model capable of producing a cohesive zone between a droplet and a fibre requires a strain sensor for accurate strain and stress–strain derivative data.

Declaration of competing interest

No author associated with this paper has disclosed any potential or pertinent conflicts which may be perceived to have impending conflict with this work. For full disclosure statements refer to https://doi.org/10.1016/j.compscitech.2020.108163.

Acknowledgements

This project has received funding from the European Union's Horizon 2020 research and innovation programme under the Marie Skłodowska-Curie grant agreement No 764713. Authors want to acknowledge P. Laurikainen for assistance in experiments and CSC – IT Center for Science (Finland) for computational resources. This work made use of Tampere Microscopy Center facilities at Tampere University.

References

[1] M. Zhang, B. Sun, B. Gu, Meso-structure ageing mechanism of 3-D braided composite's compressive behaviors under accelerated thermo-oxidative ageing environment, Mech. Mater. 115 (1) (2017) 47–63.

[2] S. Korkiakoski, P. Brondsted, E. Sarlin, O. Saarela, Influence of specimen type and reinforcement on measured tension–tension fatigue life of unidirectional GFRP laminates, Int. J. Fatigue 85 (2016) 114–129.

[3] S. Zhandarov, E. Mäder, Characterization of fiber/matrix interface strength: applicability of different tests, approaches and parameters, Compos. Sci. Technol. 65 (1) (2005) 149–160.

[4] B. Miller, P. Muri, L. Rebenfeld, A microbond method for determination of the shear strength of a fiber/resin interface, Compos. Sci. Technol. 28 (1) (1987) 17–32.

[5] L. Yang, J. Thomason, Interface strength in glass fibre–polypropylene measured using the fibre pull-out and microbond methods, Composites A 41 (9) (2010) 1077–1083.

[6] C. Zhi, H. Long, M. Miao, Microbond testing and finite element simulation of fibre-microballoon-epoxy ternary composites, Polym. Test. 65 (2018) 450–458.

[7] P. Davies, B. Blackman, A. Brunner, Standard test methods for delamination resistance of composite materials: current status, Appl. Compos. Mater. 5 (6) (1998) 345–364.

[8] F.J. Chaves, L. Da Silva, M. De Moura, D. Dillard, V. Esteves, Fracture mechanics tests in adhesively bonded joints: a literature review, J. Adhes. 90 (12) (2014) 955–992.

[9] S. Zhandarov, E. Mäder, Determining the interfacial toughness from force–displacement curves in the pull-out and microbond tests using the alternative method, Int. J. Adhes. Adhes. 65 (2016) 11–18.

[10] S. Sockalingam, M. Dey, J.W. Gillespie Jr, M. Keefe, Finite element analysis of the microdroplet test method using cohesive zone model of the fiber/matrix interface, Composites A 56 (2014) 239–247.

[11] M. von Essen, E. Sarlin, O. Tanhuanpää, M. Kakkonen, P. Laurikainen, M. Hoikkanen, R. Haakana, J. Vuorinen, P. Kallio, Automated high-throughput microbond tester for interfacial shear strength studies, in: The SAMPE Europe Conference, Stuttgart, Germany, Held in November 14–16, 2017.

[12] X. Gu, R. Young, Deformation micromechanics in model carbon fiber reinforced composites part II: The microbond test, Text. Res. J. 67 (2) (1997) 93–100.

[13] J. Ash, W. Cross, D. Svalstad, J. Kellar, L. Kjerengtroen, Finite element evaluation of the microbond test: meniscus effect, interphase region, and vise angle, Compos. Sci. Technol. 63 (5) (2003) 641–651.

[14] E. Mesquita, L. Pereira, A. Theodosiou, N. Alberto, J. Melo, C. Marques, K. Kalli, P. André, H. Varum, P. Antunes, Optical sensors for bond-slip characterization and monitoring of RC structures, Sensors Actuators A 280 (2018) 332–339.

[15] A. Johnson, F. Zhao, S. Hayes, F. Jones, Influence of a matrix crack on stress transfer to an α-alumina fibre in epoxy resin using FEA and photoelasticity, Compos. Sci. Technol. 66 (13) (2006) 2023–2029.

[16] R. Dsouza, P. Antunes, M. Kakkonen, J. Jokinen, E. Sarlin, P. Kallio, M. Kanerva, Experimental and numerical dataset of Microbond test using optical fibres for strain, Data in Brief (2020). submitted for publication.

[17] G. Alfano, On the influence of the shape of the interface law on the application of cohesive-zone models, Compos. Sci. Technol. 66 (6) (2006) 723–730.

[18] R. Scheer, J. Nairn, A comparison of several fracture mechanics methods for measuring interfacial toughness with microbond tests, J. Adhes. 53 (1–2) (1995) 45–68.

[19] R. Dsouza, J. Jokinen, E. Sarlin, P. Antunes, M. Kanerva, et al., Future microbond testing-finite element simulation of optical fibers for strains, in: ICCM22 2019, Engineers Australia, 2019, pp. 3730–3741, ISBN 9781925627220.

[20] G. Nian, Q. Li, Q. Xu, S. Qu, A cohesive zone model incorporating a Coulomb friction law for fiber-reinforced composites, Compos. Sci. Technol. 157 (2018) 195–201.